



ELSEVIER

Contents lists available at ScienceDirect

Nuclear Instruments and Methods in Physics Research A

journal homepage: www.elsevier.com/locate/nima

First testing of the CALIFA Barrel Demonstrator



B. Pietras^{a,*}, M. Winkel^b, H. Alvarez-Pol^a, M. Bendel^b, E. Casarejos^c, J. Cederkäll^d,
D. Cortina-Gil^a, G. Fernandez^e, R. Gernhäuser^b, P. Golubev^d, D. González^a, A. Hartig^e,
P. Izquierdo^c, P. Klenze^b, T. Le Bleis^b, E. Nácher^f, A. Perea^f, P. Remmels^b, G. Ribeiro^f,
P. Teubig^g, J. Vilan^c, P. Yañez^c

^a Dpt. de Física de Partículas, Universidade de Santiago de Compostela, E-15782 Santiago de Compostela, Spain

^b Technische Universität München, 80333 Garching, Germany

^c Universidade de Vigo, E-36310 Vigo, Spain

^d Department of Physics, Lund University, Box 118, SE-221 00 Lund, Sweden

^e Institut für Kernphysik, Technische Universität Darmstadt, D-64289 Darmstadt, Germany

^f Instituto de Estructura de la Materia CSIC, Madrid, Spain

^g Centro de Física Nuclear da Universidade de Lisboa, 1649-003 Lisbon, Portugal

ARTICLE INFO

Article history:

Received 14 April 2015

Received in revised form

20 December 2015

Accepted 11 January 2016

Available online 21 January 2016

Keywords:

Calorimetry

Caesium iodide

Scintillator materials

CALIFA

R³B

Avalanche photodiodes

ABSTRACT

Advancement of the CALIFA calorimeter project has reached a new milestone with the construction of the first modules of the CALIFA Demonstrator, ultimately to be integrated into the final calorimeter. Aspects and methods of detector optimisation will be discussed, along with characterisation using proton beams of $70 < E_{kin} < 230$ MeV at the Bronowice Cyclotron Centre (CCB) in Krakow, Poland. Features such as the support structure, crystal geometry and digital electronics represent the final versions to be employed, enabling a full test of each component's performance. A study of caesium iodide quenching over the available proton energy range has been performed, to accompany a method for proton calibration scaled from the measured gamma-ray energies.

© 2016 Elsevier B.V. All rights reserved.

1. Introduction

The forthcoming Facility for Antiproton and Ion Research, FAIR [1] heralds the arrival of a new field of nuclear physics exploration, with the most exotic, unstable heavy nuclei available to study within the R³B (Reactions with Relativistic Radioactive Beams) physics programme [2]. A deep probe of the nuclear structure of these exotic species requires beam energies corresponding to $\beta \simeq 0.82$, yielding reaction kinematics under the strong influence of relativistic effects.

The complete recovery of the centre-of-mass frame energy of particles emitted during in-flight reactions at the R³B setup presents a number of challenges. Heavier reaction fragments will be identified downstream, with the lighter particles along with prompt decay γ rays emitted within the larger angular range covered by the CALIFA calorimeter (CALorimeter for In-Flight

emitted pArticles). Angular segmentation must be tailored to reduce the post-correction Doppler broadening contribution for the reconstruction of gamma rays in flight, to below 4% at 1 MeV, to meet the $(\Delta E/E) < 6\%$ requirement of the R³B physics programme [3]. A huge dynamic range must be accessible; from 100 keV gamma rays to 320 MeV protons.¹ Finally, the absolute efficiency for the detection of γ rays with energies up to $E_g < 15$ MeV in the laboratory frame must be as high as possible for calorimetric measurements, requiring a minimum of dead material. These conditions have been met by the CALIFA calorimeter, separated into two sections: the Barrel [4] and the Endcap [5], covering the angular ranges $140.3 < \theta < 43.2$ and $43.2 < \theta < 7.2$ degrees respectively. This paper addresses performance of the Barrel Demonstrator detector petals, a modular fraction of the Barrel section of the calorimeter, which features all components envisaged for the final detector. The maximum capacity of the

* Corresponding author.

E-mail address: benpietras@protonmail.ch (B. Pietras).

¹ This refers to the kinematical range of the Barrel section.

Barrel Demonstrator is 12 petals, each petal holding a 4×16 array of 64 crystals within a carbon fibre alveoli support structure. Two petals have been presently constructed and tested; the results presented in this paper. These petals will ultimately be integrated as part of the Barrel section of the final detector. A schematic of the Barrel Demonstrator and a recent installation for a test experiment at GSI in Darmstadt may be seen in Fig. 1.

In order to reduce dead material within the calorimeter, a bare 300 μm thickness of carbon fibre is used for the 'honeycomb' alveoli support structure, aiming to utilise the absolute minimum material required to maintain a stable support. This is vital to optimise detector efficiency and reduce energy straggling effects, and is the result of an extensive R&D campaign [4,6,7]. The support structure is held within an aluminium casing, employing a modularised version of the same supportive infrastructure intended for the final calorimeter design. The crystals themselves have various lengths, with longer crystals required for the higher particle and γ -ray energies present at lower post-target polar angles. Each petal consists of 24×220 mm, 24×180 mm and 16×170 mm CsI:Tl crystals. In Fig. 2 representations of a petal may be seen, depicting the interior carbon fibre support structure. The alveoli, each holding a packet of four crystals in place, are aligned in the azimuthal direction to provide a ring structure which will enable a uniform angular uncertainty for any given azimuthal angle in the final calorimeter setup. The petals feature a removable side panel for increased ease of access to the internal crystals [8]. Features such as the aluminium 'tiles', which will form the exoskeleton of the Barrel section, and the 'fingers', each of which secures four crystals inside each alveoli, are also highlighted in the figure.

The crystals are coupled to large area avalanche photodiodes (LAAPDs), the Hamamatsu S12102 model comprised of two 10 mm² APDs in a common ceramic frame, the result of a research partnership of the collaboration with the manufacturer Hamamatsu [9]. The signal from the APDs is passed to the recently produced MPRB-32 preamplifier modules, directly mounted to the tile covers of the petals. The MPRB-32 is the result of a further research partnership between the CALIFA collaboration and Mesytec [10]. The amplified signal is then passed on analogue differential lines to the FEBEXv3 'Front End Board with optical link Extension'. These FPGA 'field-programmable gate array' based digital electronics, developed by our collaboration partner from GSI in Darmstadt, feature 16 channels per card and resources for substantial real-time analysis [11].

2. Component optimisation

To meet the demanding requirements of the R3B physics programme, every contributory aspect to detector performance must be painstakingly optimised. The following section will detail such efforts undertaken as regards the following components: the scintillation crystals, the photosensor, the optical wrapping and coupling and the support structure.

The foundation of every calorimeter is the active element employed to detect the incident radiation. The scintillator material caesium iodide doped with thallium (CsI:Tl) was determined to fulfil the requirements, with the Amcryst-H Ltd. [12] selected as the manufacturer of the highest quality crystals among five candidates [13]. Inherent to the Czochralski method used in production of the

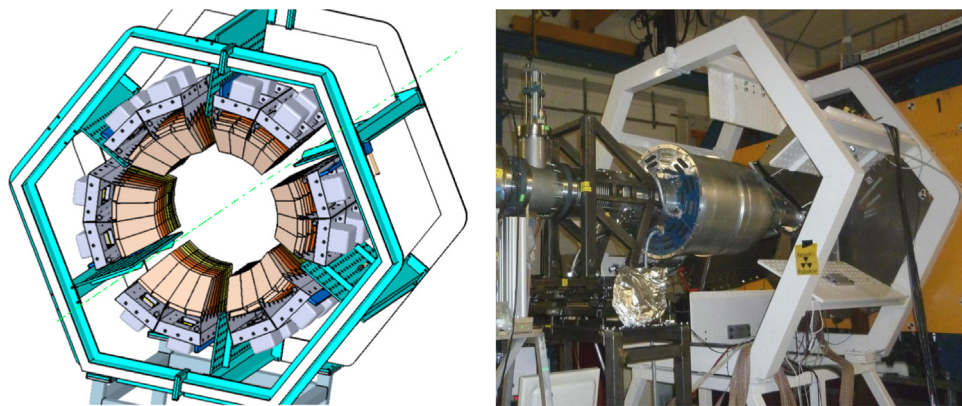


Fig. 1. Left: schematic of the Barrel Demonstrator detector consisting of 12 petals, of which two are presently constructed. Right: the Barrel Demonstrator at Cave C, GSI, for a recent experiment. Each petal holds 64 CsI:Tl crystals, with geometries corresponding to the forthcoming CALIFA calorimeter.

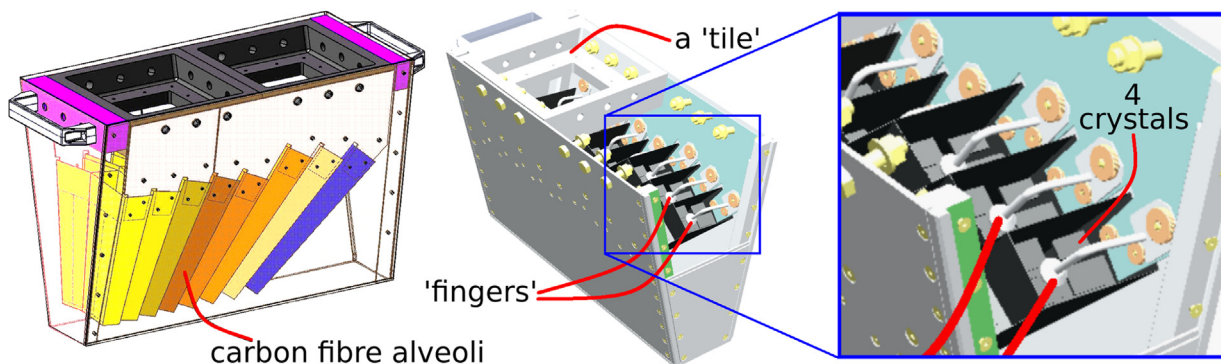


Fig. 2. Left: a schematic of petal, highlighting the interior carbon fibre support structure, which holds 64 crystals, 4 to each alveoli pocket. Right: a further petal schematic, which illustrates the 'fingers' used to support the exit face of the crystals, as well as a 'tile' at the top of the petal, which are designed to tessellate to form the exoskeleton support of the final calorimeter.

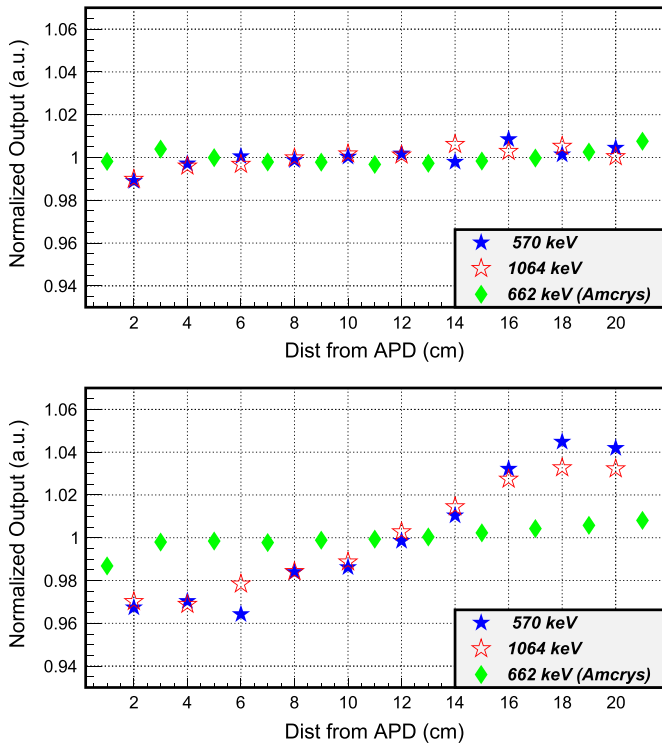


Fig. 3. Light output non-uniformity measurement for a superior (top figure) and inferior (bottom figure) 220 mm crystal. Two peaks were taken from a slit-collimated ^{207}Bi source, acting as a self-confirmation for each measurement. Measurements were taken at 20 mm intervals across the crystals, with a 5 min acquisition live-time for each point. Shown also are the LONU measurements from the manufacturer, Amcrlys-H Ltd, taken using a photo multiplier. A database of the measurements of 150+ crystals has been compiled to date.

large CsI:Tl boules, there exist slight slopes of dopant and trace contaminant concentrations along the crystal length. These slopes need to be reduced to an absolute minimum in order to maintain good energy resolution when high energy gamma rays scatter through a multitude of crystals. One effect of such slopes is, together with focussing and absorption effects in long crystals [14], reflected in the light output non-uniformity (LONU), which may be measured by irradiating different sections of the crystal with a collimated source. To this end, a test bench was constructed to automate the measurement process. Each of the 128 crystals was selected for use in the two existing petals following the test bench measurement, with an example of both a superior (top figure) and an inferior (bottom figure) crystal shown in Fig. 3. Shown also are the LONU measurements made by the manufacturer, Amcrlys-H Ltd, measured using a silicon pad as an airtight interface between the crystal and a photo multiplier. Slight inhomogeneities within the CsI:Tl boules may account for such variations in crystal performance.

The crystals were measured following mounting with the S12102 APDs. The light uniformity was generally found to be very good over the range of the crystals. This measurement was found to be very sensitive to the quality of the reflective wrapping of the individual crystals. The energy resolution measurement of an isolated crystal was found to be poor: in the region of $\Delta E/E=9\%$ at 1 MeV. This was determined to be a consequence of the wrapping. ESR [15], an ‘Enhanced Specular Reflector’, was selected following an extensive R & D campaign [7]. It is a brilliant reflector, however even when tightly wrapped, its slight plastic rigidity results in the wrapping-crystal contact points typically being at the edges of a single crystal. This issue is resolved naturally, when the wrapped crystals are placed within the carbon fibre alveoli holding structure, the tight grid configuration ensuring the ESR lies flush to the

faces of the crystal. This seemingly trivial effect reduces the vast majority of crystal’s energy resolution to under 6% at 1 MeV. As an aside, the wrapping configuration determined to be most effective consisted of two pieces of ESR, one a single frame surrounding the LAAPD, the other folded around the remaining 5 faces as a sheath.

The S12102 APDs were previously characterised by the company, matching 10 mm² single APDs to pair for similar optimum bias voltage, then applying the average as a common bias to each 10 × 20 mm unit. The combination of LAAPDs with CsI:Tl has a number of essential advantages: good energy resolution, a compact construction, a dynamic range which can handle the 0.1–350 MeV requirements, a quantum efficiency matching well to the ~550 nm light output of the CsI:Tl [16,17] and impervious to the magnetic fringe fields created by close proximity to GLAD, the superconducting dipole magnet of the R3B experimental setup. A further area for optimisation was the optical cement used to affix the LAAPDs to the crystals. In previous prototypes [18] the affixing agent used was RTV 861, an epoxy adhesive from Scionix. While satisfactory, the refractive indices used with this cement (crystal-optical cement–APD silicon window) are 1.79–1.45–1.55, which indicates that internal reflection of the scintillation light may be reduced. A number of candidates [19] were subsequently tested, with Melmount 1.704 [20] (named after its refractive index) as a thermoplastic liquid at 70 °C, offering the advantage of easily re-affixing the APD should it become detached. Testing ultimately yielded Epotek 301-2 [21] with a refractive index of 1.57 as the superior choice, to be used in future petal construction. So the optimum solution in this case was an optical adhesive where the index of refraction best matches the APD window and therefore minimises the loss of light at the interface. The gamma energy resolution in each case was measured for two petals, the results from 128 crystals shown are in Fig. 4. Effects of long-term ageing of the adhesive are uncertain [22], though the moderate hygroscopicity of caesium iodide is considered, with a steady flow of dry nitrogen into the petals at a maximum rate of 10 l/h employed as a flushing gas to protect the crystals against humidity.

3. Detector electronics

Receiving the signal from the APDs are the MPRB-32 Mesytec preamplifiers, essentially two MPRB-16 preamplifiers in a single module, specifically developed for the CALIFA project. The APDs have a temperature dependent gain of $-2.8\%/^{\circ}\text{C}$ over the range 22–24 °C [4]. To overcome this effect, the preamplifiers incorporate an on-the-fly temperature-gain correction implemented by an adjustable linear correction in the bias voltage for the sensors, keeping the signals stable over a limited temperature range. The effect can be seen in Fig. 5, where the temperature was varied measuring a ^{137}Cs source, both with and without the temperature-gain correction [4].

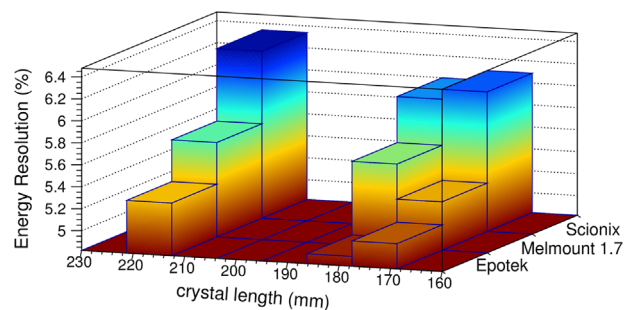


Fig. 4. Energy resolution dependence on both crystal length and optical adhesive.

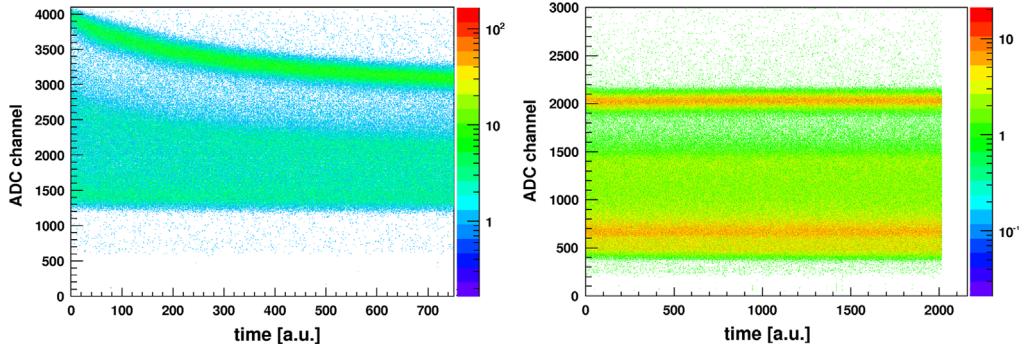


Fig. 5. Left: spectrum of a ^{137}Cs source detected with a CsI:Tl crystal, showing the gain gradient due to continuous heating of the Hamamatsu S8664-1010 LAAPD from 11.3 to 22.7 °C. Right: same as *left*, but in the range of 6– 24 °C with the temperature – gain correction applied [4].

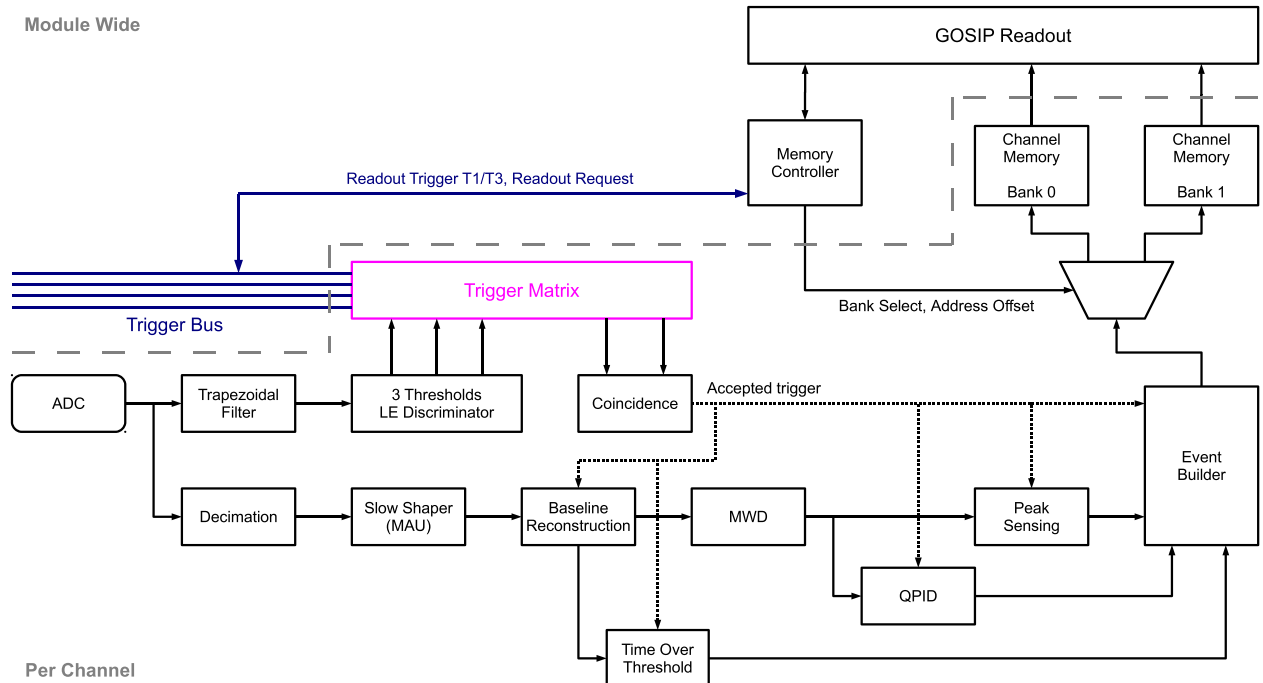


Fig. 6. Processing scheme for the FEBEX-GOSIP digital electronics, where steps such as the moving window deconvolution ‘MWD’, moving average unit ‘MAU’, constant fraction discriminator ‘CFD’ and Quick Particle IDentification stage ‘QPID’ are indicated.

The potential of caesium iodide for particle identification is long established [23], the fast and slow decay constants of caesium iodide (~ 0.6 and $\sim 3.3 \mu\text{s}$ respectively) yielding a ratio corresponding to the ionisation density of the absorbed particle. This ratio can be used to identify the particle type by use of pulse shape analysis (PSA), e.g. using the ‘Quick Particle IDentification’ (QPID) algorithm [24]. The PSA is done in real-time on the FEBEX boards, thus minimising the data output to the readout [25]. This setup is already the same as envisioned for the final calorimeter. The analogue preamplifier signals covering a range of $U_{out} = \pm 1.2 \text{ V}$ are fed into the digital electronics, based on the 16 channel FEBEX FPGA boards [11]. The signal is digitised with a 14 bit ADC resolution at 50 MHz, with the data acquisition managed by the Multi-Branch System data acquisition system, MBS [26]. A depiction of the FEBEX system processing scheme, developed as a dedicated firmware for the CALIFA project, may be viewed in Fig. 6.

After the preamplifier signal is digitised in the sampling ADC it is converted from a continuous analogue function to a digital time-discrete function, time segmented in multiples of the sampling interval. Triggers are digitally generated via the subtraction of two short integration windows, delivering the slope at the beginning of an event signal and producing the trigger when a threshold is

exceeded. To derive the total signal amplitude as a measure for the energy deposited in the detector elements, the signals have to be treated differently in a parallel digital path. Following the baseline reconstruction, the exponential decay introduced by the pre-amplifier must be removed. This is achieved via use of the Moving Windows Deconvolution ‘MWD’ algorithm, providing the total charge function for the event. Peak sensing may then be employed to determine the energy of the event, with a further functionality provided by Quick Particle IDentification stage ‘QPID’ [24], which utilises pulse shape analysis to determine the particle type in real-time, by measuring the ratio of the fast N_f and slow N_s integrated luminescences, where $N = N_f + N_s$, with N being the total charge produced by the scintillation light.

3.1. Preamplifier gain characterisation

When digitising a signal the number of bits used to cover the full dynamic signal range is very important and may affect energy resolution. If the 14 bit ADC of the FEBEX is used to measure a proton of $E_{max} = \sim 300 \text{ MeV}$ ($\sim 18 \text{ keV/ch}$) it means that one uses only ~ 6 bits to measure a gamma ray of $\sim 1 \text{ MeV}$. This limitation may be overcome by having a ‘high’/‘low’ range setting on the

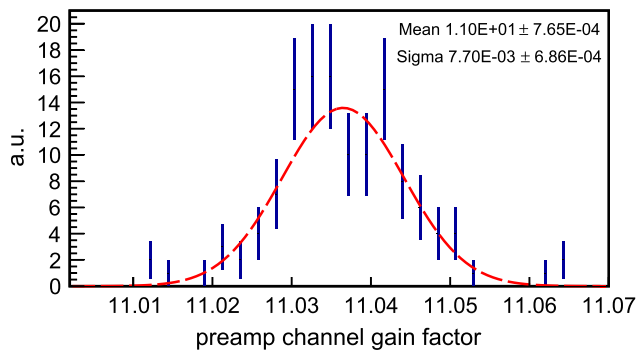


Fig. 7. The gain shift of 128 MPRB-32 channels, when fitting a set of pulser inputs with low and high gain preamplifier settings.

Mesytec MPRB-32 preamplifier to focus on the physics case of interest or double the number of signal channels. The different ranges have a nominal gain factor difference of $g_{lo}/g_{high} = 1/10$, as stated by the manufacturer. To verify this gain factor a digital pulse generator was employed over four MPRB-32 modules, totalling 128 channels. The pulser creates a signal that corresponds to the integrated light output of CsI:TI, with two decay time constants of 600 ns and 3300 ns for each event. The pulser input of the MPRB is AC coupled, so the signal is differentiated at this stage and a realistic current signal is injected to the charge integrating first stage of the MPRB-32 module. The pulse height of the integrated charge signal from the pulser is measured as a voltage proportional to the amount of the integrated charge, for more details see [27]. To calibrate the preamplifier gain setting arbitrary voltages of ~ 300 , ~ 400 , ~ 500 , ~ 600 mV were applied to the preamplifiers for both the high and low range setting. The high and low points for each voltage were then plotted against each other and a linear fit applied, with the offset fixed at zero. The 128 slopes of this fit can be seen in Fig. 7, with a Gaussian mean value (σ) of 11.04 ($7.7E-03$). Although a little higher than the nominally stated $g_{high}/g_{low} = 10$, the small sigma value reflects the uniformity of the preamplifier channels. The individual measurement of the preamplifier gain factors is required to enable the proton energy measurements to be described in units of the light output from a set gamma-ray energy, as will be detailed in Section 6.

4. Experimental testing

Offering proton therapy beams adjustable from 70 to 230 MeV, the 'Proteus C-235' proton cyclotron at the Bronowice Cyclotron Centre (CCB) in Krakow [28] is an ideal facility to characterise the newly constructed Demonstrator petals. The proton beam was scattered off a 50 μm thick titanium foil, which also served as the endcap to the vacuum beam pipe, shown in Fig. 8. Most of the protons elastically scattered from the titanium foil enter the crystals through their front face and their path along the long crystal axis is stopped within the active volume, even for the shortest crystals of length 170 mm. The crystals display an overall good energy resolution, more so for the shorter crystals. This is most likely due to factors such as light transport and light absorption within the crystal volume, in addition to a typically better light output non-uniformity for the shorter crystals, as the range in which LONU may occur is reduced. The energy distribution of the beam was guaranteed to be less than 0.7%, which has been accounted for in the energy resolution values shown in Fig. 9.

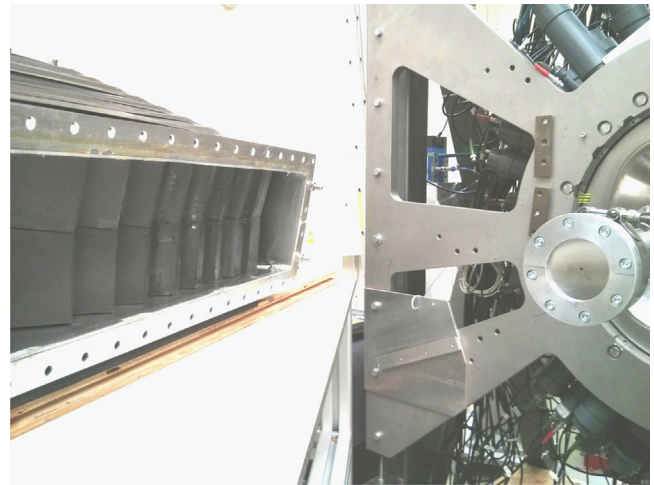


Fig. 8. Proton beams scatter off the 50 μm titanium foil to enter the crystals held within the carbon fibre support structure of the petal.

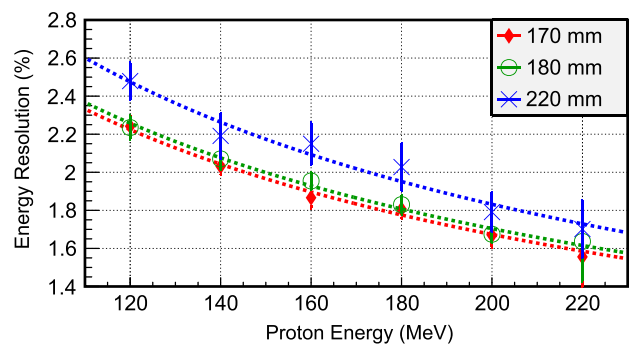


Fig. 9. The average proton full width half maximum energy resolution $\Delta E/E$ for 170, 180 and 220 mm length crystals. The error bars represent the standard deviation of the range of measurements contributing to each average value.

5. Proton calibration method for CALIFA

Proton calibration is trivial with access to a range of mono-energetic proton beams, but how may it be achieved for the complete CALIFA calorimeter when resident at FAIR? Previous prototype testing at the CCB, Krakow, Poland, suggested a fixed relation between gamma and proton calibration slopes. With 64 channels, a Demonstrator petal presented an excellent means to investigate this possibility.

Firstly, the use of a rare $^{13}\text{C} + ^{244}\text{Cm}$ source enabled the gamma calibration to span 0.511–6.13 MeV – this wide energy range being of great benefit to the following procedure. When employing a standard linear function the gamma calibration offset was found to be negligible using the digital analysis methods described before, so was fixed at zero for each fit.

Secondly, each crystal was calibrated using proton beams with nominal energies of 120, 140, 160, 180, 200 and 220 MeV. The energy lost while passing through a 50 μm titanium foil target as well as the energy dependence on the elastic scattering angle (theta) was accounted for by use of a GEANT4 simulation, the values for the centre of each crystal entrance face displayed as dotted lines in Fig. 10. As may be seen, there is a $\sim 0.1\%$ loss when passing through the scattering foil, with the energy loss across the detector array angular range from 99.28 to 99.76%. The energy loss through the 34.8 cm air-gap, 300 μm carbon fibre alveoli and 65 μm ESR wrapping were also accounted for [29].

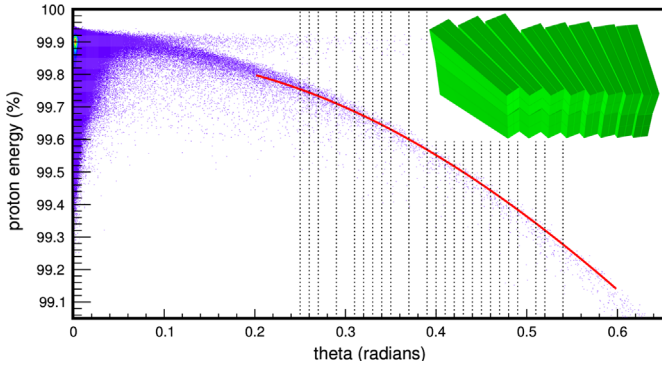


Fig. 10. A GEANT4 simulation of the experimental setup, showing the angular dependence of the proton energy following elastic scattering from the 50 μm titanium foil. Dotted lines mark the centre of each crystal entrance face in the array. The insert, top right, shows a GEANT4 model of the crystal geometry.

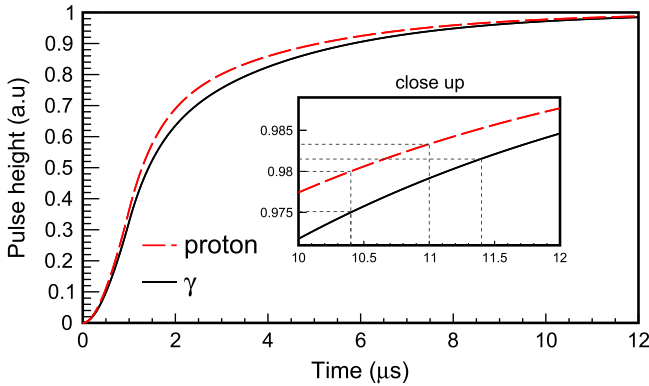


Fig. 11. Normalised integrated light collection over time for both a proton and a gamma-ray event. Straight lines on the zoomed area refer to the specific values of our FEBEX settings, shown in Table 1.

Table 1

Charge integration time for γ and proton events.

Integration time (μs)	Proton pulse (%)	γ pulse (%)
10.4	98	97.5
11.0	98.33	N/A
11.4	N/A	98.15

5.1. Light collection window effects

An optimum light collection window is long enough to collect the bulk of the pulse, without collecting the tail region where noise begins to dominate the signal. To understand the importance of different charge integration times it is relevant to examine the effect of the signal collection window, by plotting the normalised light production over time for both a proton and a gamma-ray event, see Fig. 11. The percentage of the light pulse collected for our FEBEX settings can be seen in Table 1.

5.2. Proton – γ ray energy calibration scaling

If these values are applied to both gamma and proton calibrations,² then the points may be combined. As the gain factor for each preamplifier channel was measured with the pulser calibration, this ~ 11.04 factor may also be accounted for on a channel-by-channel basis, converting the gamma-ray energy

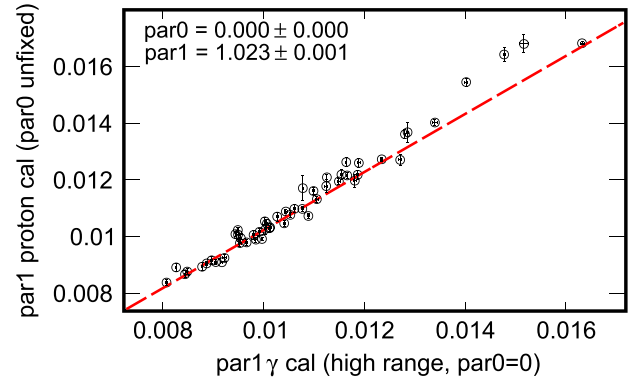


Fig. 12. A common relation between gamma and high energy proton energy calibration slopes in caesium iodide, following both a gain and a pulse fraction correction for the charge integration time used for each measurement. The gamma energies were measured in the low range setting of the preamplifier, then converted to the high range values in channels using the pulser gain calibration. The best linear fits for both protons and gammas were taken, 53/64 crystals here shown.

peaks to their equivalent value in channels for the high range setting of the preamplifier. Once this is done, both the proton and the gamma measurements may be calibrated using a linear fit. For the gamma calibration, the offset was negligible and so fixed at 0. The proton offset was initially left unfixed. The slopes of the gamma and proton calibration for 53 crystals³ following both the gain and pulse fraction correction may be seen in Fig. 12.

As the physical process underlying gamma-ray and proton interaction within the scintillator is markedly different [30], the correlation is quite astounding. A linear fit of the respective calibration slope parameters (the offset of *this* fit fixed to zero) yielding a slope of 1.023 ± 0.001 . In order to better constrain the fit, the proton linear energy calibration was refitted with the offset fixed at -14 , as this was the value which provided the lowest average χ^2/ndf over a range of fixed offset values.

The slopes for each crystal's proton calibration were derived from the method above, as shown in Eq. (1). The proton calibration offset, p_0 , was set as -14 , as this fixed value yielded the minimum χ^2/ndf .

$$p1_p = p1_{gHR} \cdot SF \quad (1)$$

where $p1_p$ is the proton calibration slope, $p1_{gHR}$ is the slope of a linear gamma calibration after the gamma energies have been converted to the preamplifier high range setting (with the offset of the linear fit fixed at zero) and SF is the scaling factor, which has a dependence on the fixed offset value of the proton linear fits. The value of -14 to fix the proton calibration as shown in Fig. 13 gave $SF=1.022$, however values -17 to -10 were also tested. The relation between the fixed proton linear fit offset value and the scaling factor may be seen in Fig. 14.

To test this method, the proton calibration derived using Eq. (1) was applied to each raw channel. Energy residuals were then measured by subtracting the measured calibrated value from the nominal energy value for 55 channels. This was also performed for the same channels using a calibration extracted directly from the proton energy measurements (without fixed linear fit parameters). In all cases the effects of pre-crystal proton energy loss, proton scattering angle and the charge integration time were accounted for. The results for each case may be seen in Fig. 15. The offset p_0 was taken as -14 with a scaling factor of 1.022 for the case shown in the upper section of Fig. 15, however using any value shown in Fig. 14 gave comparable residuals.

² For example a correction of $1/0.975$ is applied to the γ Gaussian Mean for the first FEBEX card, etc.

³ The superior crystals are measured.

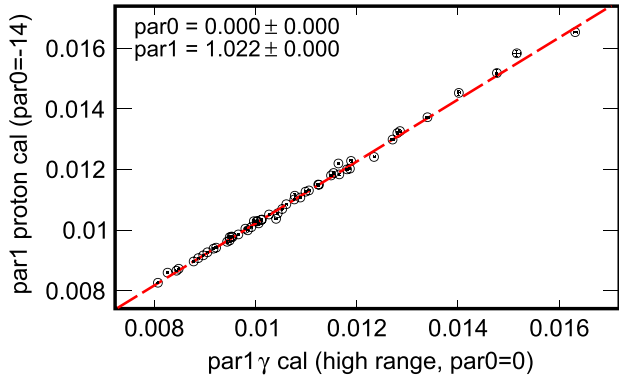


Fig. 13. The same measurement as displayed in Fig. 12, except for the proton energy linear fit had the condition that the offset was fixed at -14 .

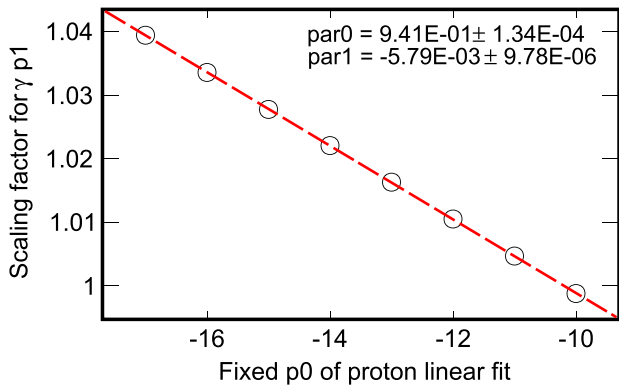


Fig. 14. The γ -proton high-range scaling factor found when varying the fixed offset value for the proton linear energy calibration.

6. Caesium iodide quenching

An interesting question is the underlying physical cause of the factor S_{gp} 1.023 ± 0.001 found in Fig. 12. Similar to the work of Koba et al. [31] the proton energy measurements were converted into units of light output corresponding to the light measured for a 0.662 MeV γ ray decay from ^{137}Cs . In order to directly compare our measurements to this data, a linear fit was performed to find the equivalent uncalibrated value at 0.662 MeV for each crystal, this value being used as the light output unit. As there was a change in the preamplifier gain setting from 'low' for the gamma-ray measurements to 'high' for the proton measurements, the measured high-low gain factor for each preamplifier was removed channel-by-channel using the data displayed in Fig. 7.

To determine the average energy loss per unit distance, dE/dx , for each proton energy in caesium iodide, the Bethe–Bloch formula was employed [32]. This formula, shown in Eq. (2), describes the energy loss per distance travelled of charged particles traversing matter, e.g. a measure of the stopping power of the material.

$$-\frac{dE}{dx} = 4\pi r_0^2 z^2 \frac{m_e c^2}{\beta^2} N Z \left[\ln \left(\frac{2m_e c^2}{I} \right) - \ln(1 - \beta^2) - \beta^2 \right] \quad (2)$$

where r_0 is the classical electron radius, z is the charge of the incident particles, $m_e c^2$ is the rest mass energy of the electron, Z is the atomic number of material, N is the atomic density of material and I is the mean excitation potential. As the proton energies considered were over 100 MeV, shell effects may be discounted, as may density effects which increase in significance at very high energies. The Bethe–Bloch formula was used to create the data for energetic protons traversing caesium iodide, displayed in Fig. 16. On the left axis is the total proton energy lost against the

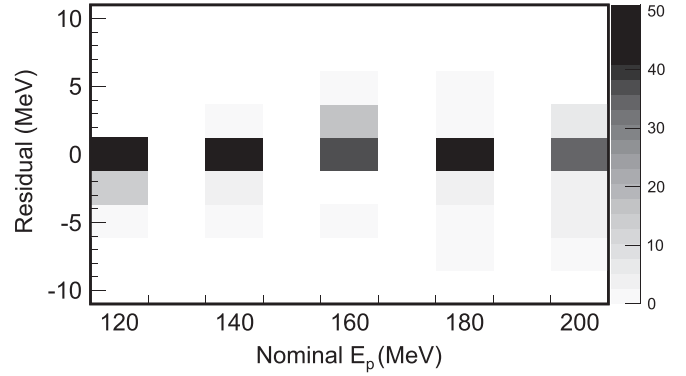
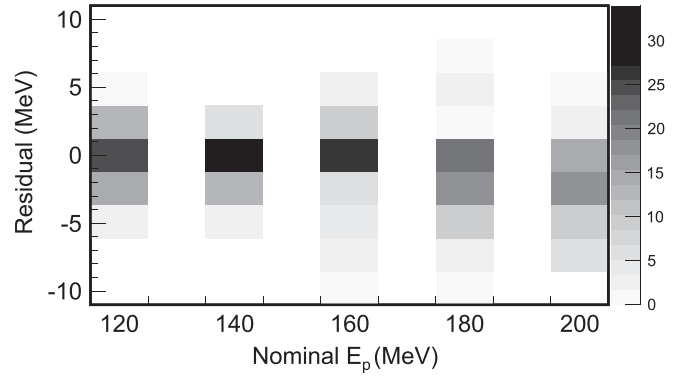


Fig. 15. Upper: the proton energy residuals measured for 55 crystals (51 for 200 MeV), following a linear proton energy calibration using slopes taken from Eq. (1) and -14 as the offset (i.e. based on the gamma-ray energy calibration). Lower: residuals resulting from a native proton energy calibration for the same channels.

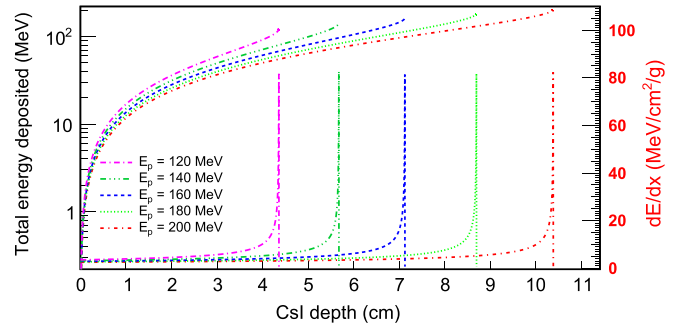


Fig. 16. Shown on the left axis is the total proton energy lost as the protons penetrate the caesium iodide. On the right axis is displayed the rate of energy deposition which terminates in the Bragg peaks for the respective proton energies.

penetration distance inside the caesium iodide. On the right axis is displayed the rate of energy deposition which terminates in the proton energies' respective Bragg peaks.

The luminescence per unit length may be described as a function of stopping power, as shown in the following equation:

$$\frac{dL}{dx} = \frac{S(dE/dx)}{1 + kB(dE/dx)} \quad (3)$$

where S is the absolute scintillation efficiency and kB is the Birks parameter [33]. Eq. (3) describes how the amount of the luminescence per unit length decreases due to a quenching effect in the high dE/dx region. The dependence of scintillation efficiency (dL/dE) on the energy loss per unit distance (dE/dx) is described by the following Birks equation:

$$\frac{dL}{dE} = \frac{a}{1 + b(dE/dx)} \quad (4)$$

It should be noted that the Birks equation was derived for the properties of organic scintillators, so is not directly applicable to inorganic crystals such as caesium iodide. A modification to reproduce quenching in the low energy loss region has been proposed [31], shown in the following equation:

$$\frac{dL}{dE} = \frac{a}{1 + b(dE/dx) + c(dE/dx)^2} \quad (5)$$

The respective parameters may be found in Table 2.

Using Eq. (5) it is possible to directly calculate the light output proton–gamma ratio or ‘quenching’ for a given incident proton energy, via the integration of dE/dx over the path of the proton through the material. The formula is shown in the following equation:

$$\frac{E_p}{E_\gamma} = \frac{1}{E_{total}} \int_0^x \frac{dL}{dE} \left(\frac{dE}{dx} \right) \cdot \frac{dE}{dx} dx \quad (6)$$

where E_{total} is the nominal incident proton energy, dE/dx is the rate of energy deposition, integrated from 0 (the entry point of the proton in the material) to x (the distance at which the proton is stopped). The light output per unit energy, dL/dE , is taken from Eq. (5) and the dE/dx is obtained using the *pstar* database: based on the Bethe–Bloch formula, but including the nuclear stopping power [34]. This may be used to calculate the quenching as a function of total proton energy, as displayed in Fig. 17. The data, linearly interpolated to the nominal proton energy for each crystal and subsequently averaged, may also be seen on the figure, with the standard deviation of the mean value displayed as the error. The measured data is within errors of the calculated quenching for each point.

Shown in Table 3 are values obtained using the *pstar* database [34], for each nominal proton energy. The dL/dE values were taken from an average of the slopes between each measured light output. This method could doubtless be improved with detailed energy measurements over a range which extends to the lower energy region.

The values shown in Table 3 may be seen plotted against both the Birks and the Modified Birks functions in Fig. 18. The dL/dE values are the first derivative of a second-order polynomial fit of

Table 2
The parameters for each equation.

CsI	<i>a</i>	<i>b</i>	<i>c</i>	Eq.
Birks	1.08	1.29E–3	–	4
Modified Birks	1.26	1.92E–3	0.747	5

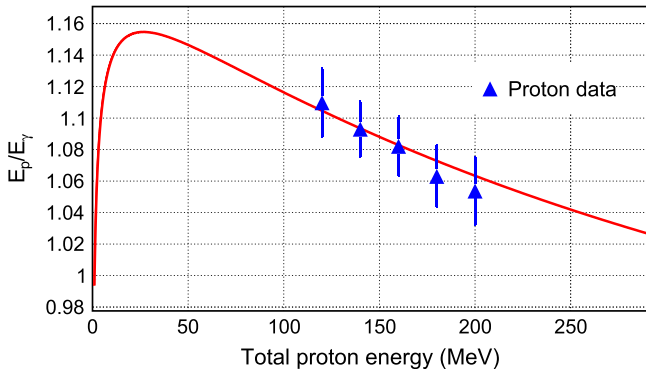


Fig. 17. The light output ratio of proton energy to gamma energy arising from an integration of the Modified Birks formula, as per Eq. (6), plotted against total proton energy. Experimental data is overlaid, giving good agreement with theory.

Table 3
Charge collected by integration time for γ and proton events.

Proton energy (MeV)	dE/dx (MeVcm ² /g)	Equivalent gamma-ray light output (MeV)	Light output (0.662/L (¹³⁷ Cs)/MeV)	dL/dE (0.662/L (¹³⁷ Cs)/MeV)	Penetration depth (cm)
120	3.548	132.697	1.10581	0.997	4.40
140	3.200	153.193	1.09424	0.979	5.72
160	2.933	173.394	1.08371	0.960	7.16
180	2.722	193.226	1.07348	0.942	8.73
200	2.551	212.800	1.06400	0.924	10.41

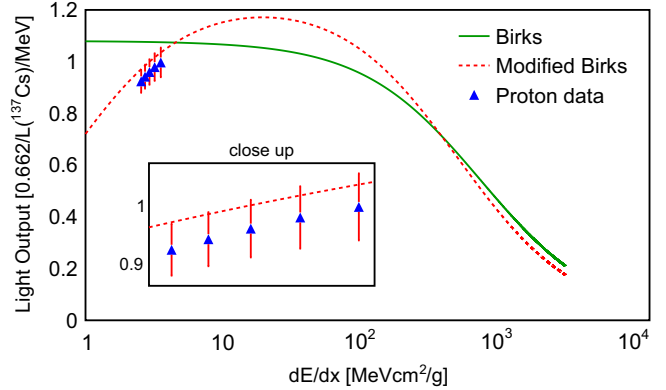


Fig. 18. Data plotted against different scintillation efficiency curves, finding agreement with the Modified Birks function within errors, the error bars representing the standard deviation of the range of measurements contributing to each average value.

the measured energy in the gamma calibration against the calculated proton energy at each proton energy.

It should be noted that a lower average dE/dx value corresponds to a higher incident energy. The higher energy quenching shown in Fig. 18 may be explained in terms of activator site availability, where the energy carriers are taken to be excitons resulting from the recombination of electron–hole pairs created in the wake of the particle. It was thought that increasingly high dE/dx could suffer from quenching as a consequence of activator saturation [35]. There is some debate concerning the importance of the dopant concentration and the quenching may be considered to be rather an intrinsic property of the ionisation density of the crystal [36–38]. The quenching at very low energies represents very high dE/dx values shown for protons below 20 MeV in Fig. 18, this may be understood as a smaller recombination probability of the reduced number of electron–hole pairs.

A factor not accounted for by the Remodified Birks function is that of δ -electrons, which may leave the primary ionisation column and travel to different sites of dE/dx which are not subject to such quenching. This factor would increase for heavier incident ionising particles and has been addressed to an extent by Pârlog et al. [39]. The caesium iodide light output measured against projectile energy may be seen in Fig. 19, where the proton energy measurements are shown alongside several energy measurements of several ions by Koba et al. [31].

The energy dependence of scintillator efficiency, as observed in Fig. 18, was found by Swiderski et al. [40], to be consistent across gamma rays, protons and deuterons when the primary ionising particle is expressed in terms of the electron equivalent energy, in turn dependent on the incident particles velocity. This independence of particle type to $dL/dE(dE/dx)$ concerning the primary ionisation column may be considered in terms of the conversion of all recoverable energy into electron motion for each particle

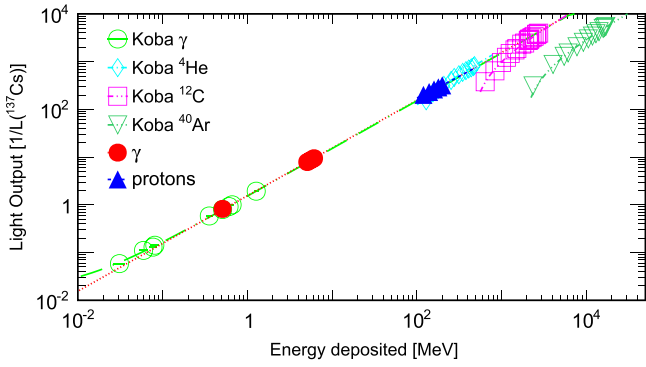


Fig. 19. The light output of CsI:TI as a function of deposited energy for gamma rays and several charged particles. The data labelled 'Koba' is taken from the second panel of Fig. 7 in [31].

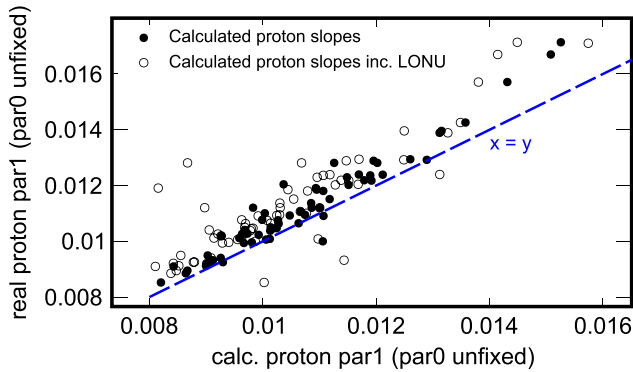


Fig. 20. Proton calibration slopes from linear fits to proton energy data compared to those calculated using an integration of the Modified Birks function, both with and without individual light output non-uniformity included. Ideally the points would fall on the $x=y$ dashed line, drawn as a visual aid.

interaction type within the scintillator. Integrating the Modified Birks function over the path of each proton to determine the dependence of quenching on incident proton energy, expressed in Eq. (6), and the gain factor for each preamplifier channel, as shown in Fig. 7, may be used to provide a proton calibration based on that of the gamma, with the channel number for each raw proton energy provided via the following equation:

$$RawE_p = gpar1 \cdot E_p \cdot GF \cdot QF(E) \quad (7)$$

where $RawE_p$ gives the uncalibrated proton energy measurement, $gpar1$ is the slope of the gamma energy calibration with the offset fixed at zero, E_p is the proton energy, GF is the preamplifier high/low gain factor for that channel (found to be ~ 11.04 in Fig. 7) and $QF(E)$ is the calculated quenching factor shown in Fig. 17. These raw channel values may then be used to make a linear proton energy fit. There is one further step we may take to extend this method. We may also use the individually measured light output non-uniformity (LONU) as displayed in Fig. 3. To do this, firstly an exponential gamma absorption through the scintillator with an attenuation length, $\mu = 0.26 \text{ cm}^{-1}$ for $E_\gamma = 1 \text{ MeV}$ [41] was assumed. After accounting for the LONU of each crystal for the gamma, the LONU effect on each proton is included for each dE/dx in the proton path via a linear interpolation between the 2 cm steps shown in Fig. 3. The lack of success of this approach may be seen in Fig. 20, where the slopes from the proton linear calibration fits are plotted against those calculated using the method detailed above, both with and without the inclusion of LONU.

It is clear from Fig. 20 that using an integrated Modified Birks function to scale up from the gamma energy calibration does not provide an accurate proton calibration, with the inclusion of the light output non-uniformity actually weakening the correlation,

which suggests light output non-uniformity may not be a limiting factor. As seen previously in Fig. 13 a common relation seems reasonable. The quenching relation still has some discrepancy to the Modified Birks function, as seen in Fig. 17.

7. APD gain-matching effect

An approach which proves most useful on experiment is the adjustment of the APD HV (the optimum typically 370–390 V) to gain-match the crystals. This is advantageous to immediately verify uniform behaviour across the crystal array, but also to modify settings within the FEBEX electronics. These settings are typically set per card; for example, the thresholds for each channel may be altered in groups of 16 – representing the input channels to each card. While convenient, this method shifts the applied APD voltage from its optimum value. For changes $< 2 \text{ V}$ this has little effect, however the relation of energy resolution to APD voltage has different minimal points. This may be seen in Fig. 21.

In Fig. 22 the effect under realistic experimental conditions may be seen, with all measurements referring to the gamma energy resolution at 1 MeV. Though the majority of crystals lose less than 1% in energy resolution when gain matched, in cases where resolution is paramount it may be useful to implement a 'pseudo-gain matching' stage, where the gain is digitally shifted without altering the optimum APD voltage applied.

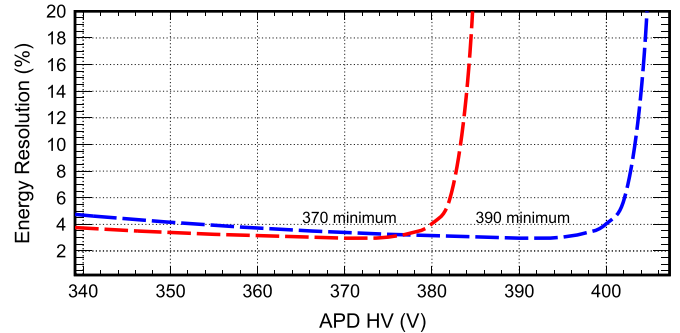


Fig. 21. The dependence of resolution upon the APD voltage applied, taken from γ -ray lab. measurements and shown for the range extremes 370 and 390 V. If gain-matching is undertaken through a shift in APD bias voltage, it is preferable to reduce rather than exceed the optimum.

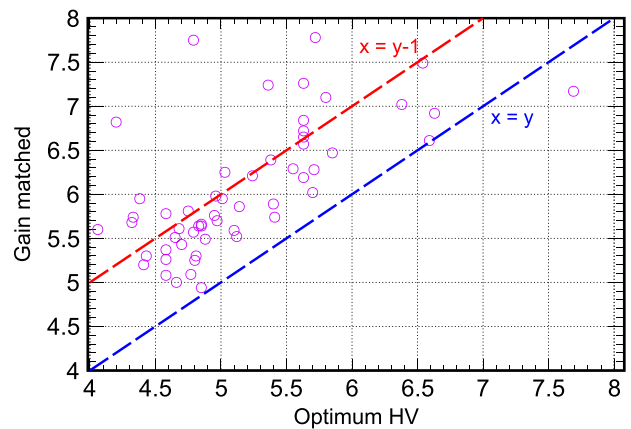


Fig. 22. The effect of gain matching the detectors, compared with using the optimum bias voltage for the APDs. All points are for the energy resolution at $E_\gamma = 1 \text{ MeV}$. Lines are included as visual aids, indicating that for the majority of crystals, using a non-optimum gain leads to an energy resolution degradation inferior to 1%.

8. Conclusions

The first detectors of the CALIFA Barrel Demonstrator have been constructed, with research and design over a range of components enabling an optimisation of energy resolution and performance. The detector was subsequently tested for gamma-ray energies ranging up to 6.1 MeV and high quality proton beams with energies ranging from 120 to 200 MeV at the Bronowice Cyclotron Centre (CCB) in Krakow, Poland. This beam-time served not only to characterise detector performance, but also to determine the suitability of the digital support electronics. A significant improvement in performance has been observed in relation to preceding prototypes, with the average energy resolution of all crystals; 170, 180 and 220 mm, reaching below 5.2% at 1 MeV gamma-ray energy. This falls nicely within the R3B physics programme requirements of 6% at 1 MeV. The response to protons exceeds the < 1% energy resolution requirement at 100 MeV, though 0.8% at 173 MeV has been achieved in previous experiments [18]. Considering the high quality of the gamma measurements, this may indicate an energy straggling factor not accounted for. The proton measurements agree well with the Modified Birks equation proposed by Koba et al. [31], but indicate there may possibly be some room for improvement with the inclusion of the effect of δ -electrons. A proton energy calibration scaled from that of the gamma's achieved residuals under 3 MeV, which should prove sufficient for a preliminary calibration.

Acknowledgements

The authors would like to thank Adam Maj (of the Henryk Niewodniczanski Institute of Nuclear Physics) for the invitation to use this marvellous facility, in addition to Bartek Szpak, for taking such good care of us during our time there.

The author is indebted also to Inés Cortés Ferro, for her kindness, patience and good humour on the experiment.

This work has been supported by the following projects MINECO (FPA2012-39404-C02-01, FPA2012-39404-C02-02, FPA2013-47831-C2-1, FPA2013-47831-C2-1, FPA2013-47831-C2-1), PRI-PIMNUP-2011-1357, Xunta de Galicia (GRC2013-11), NUPET Eranet (GANAS), ENSAR (VII PM), HIC for FAIR, BMBF (05P12WOFNF, 05P12WOFNUE, 05P12RDFN8, 05P12RDFN8), DFG (EXC153) and VR (2012-4550, 2013-2109, 2013-4178, 2014-6343).

References

- [1] The FAIR collaboration, FAIR CDR - An International Accelerator Facility for Beams of Ions and Antiprotons, Conceptual Design Report, Technical Report, GSI, 2001.
- [2] T. Aumann, B. Jonson, Technical Proposal for the Design, Construction, Commissioning and Operation of R3B. A Universal Setup for Kinematical Complete Measurements of Reactions with Relativistic Radioactive Beams, Technical Report, The R3B Collaboration, 2005.
- [3] H. Alvarez-Pol, N. Ashwood, T. Aumann, D. Bertini, P. Cabanelas, E. Casarejos, J. Cederkall, D. Cortina-Gil, P.D. Fernández, I. Duran, E. Fiori, D. Galaviz, M. Labiche, E. Nacher, B. Pietras, D. Savran, O. Tengblad, P. Teubig, Nuclear Instruments and Methods in Physics Research Section A: Accelerators, Spectrometers, Detectors and Associated Equipment 767 (2014) 453.
- [4] CALIFA/R^B Collaboration, Technical Report for the Design Construction and Commissioning of the CALIFA Barrel, Technical Report, 2012.
- [5] CALIFA/R^B Collaboration, Technical Report for the Design Construction and Commissioning of the CALIFA Endcap, Technical Report, 2014.
- [6] M. Gascón, L. Schnorrenberger, B. Pietras, H. Álvarez Pol, D. Cortina-Gil, P. D. Fernández, I. Duran, J. Glorius, D. González, D. Perez-Loureiro, N. Pietralla, D. Savran, K. Sonnabend, Journal of Instrumentation 8 (2013) P10004.
- [7] M. Gascón, Prototype of a new calorimeter for the studies of nuclear reactions with relativistic radioactive beams (PhD thesis), Universidade de Santiago de Compostela, 2010.
- [8] E. Casarejos, H. Alvarez-Pol, D. Cortina-Gil, I. Durán, A. Iglesias, P. Izquierdo, P. Yañez, J. Vilán, Design and construction of the structure of the DEMONSTRATOR of the CALIFA detector for R3B-FAIR using carbon-fiber composites, In: EPJ Web of Conferences, vol. 66, 2014, p. 11038.
- [9] Hamamatsu Photonics K.K. Solid State Division, Datenblatt Si APDS8664-series, 2005.
- [10] MPRB-32 datasheet, Mesytec GmbH & Co. KG, v2.0 edition, 2014.
- [11] GSI, FEBEXv3, (www.gsi.de/en/work/fairgsi/rare_isotope_beams/electronics/digital_electronic/digital_electronics/modules/lwl/febex/febex3a.htm).
- [12] Amcris-H, Kharkov, Ukraine, (www.amcris-h.com).
- [13] M. Gascón, H. Alvarez-Pol, J. Benlliure, E. Casarejos, D. Cortina-Gil, I. Duran, IEEE Transactions on Nuclear Science NS-55 (2008) 1259.
- [14] J. Bea, A. Gadea, L. Garcia-Raffi, J. Rico, B. Rubio, J. Tain, Nuclear Instruments and Methods in Physics Research Section A: Accelerators, Spectrometers, Detectors and Associated Equipment 350 (1994) 184.
- [15] 3M, Display films, (<http://vikuiti.com>).
- [16] M. Moszyński, M. Szawlowski, M. Kapusta, M. Balcerzyk, Nuclear Instruments and Methods in Physics Research Section A: Accelerators, Spectrometers, Detectors and Associated Equipment 485 (2002) 504.
- [17] T. Ikagawa, J. Kataoka, Y. Yatsu, T. Saito, Y. Kuramoto, N. Kawai, M. Kokubun, T. Kamae, Y. Ishikawa, N. Kawabata, Nuclear Instruments and Methods in Physics Research Section A: Accelerators, Spectrometers, Detectors and Associated Equipment 538 (2005) 640.
- [18] B. Pietras, M. Gascón, H. Alvarez-Pol, M. Bendel, T. Bloch, E. Casarejos, D. Cortina-Gil, I. Durán, E. Fiori, R. Gernhäuser, D. González, T. Kröll, T.L. Bleis, N. Montes, E. Nacher, M. Robles, A. Perea, J. Vilán, M. Winkel, Nuclear Instruments and Methods in Physics Research Section A: Accelerators, Spectrometers, Detectors and Associated Equipment 729 (2013) 77.
- [19] M. Montecchi, Q. Ingram, Nuclear Instruments and Methods in Physics Research Section A: Accelerators, Spectrometers, Detectors and Associated Equipment 465 (2001) 329.
- [20] Cargille Ltd., (<http://www.cargille.com>).
- [21] EPO-TEK Speciality Adhesives, (<http://www.epotek.com>).
- [22] J. Brose, G. Dahlinger, K. Schubert, Nuclear Instruments and Methods in Physics Research Section A: Accelerators, Spectrometers, Detectors and Associated Equipment 417 (1998) 311.
- [23] R.S. Storey, W. Jack, A. Ward, Proceedings of the Physical Society 72 (1958) 1.
- [24] M. Bendel, R. Gernhäuser, W.F. Henning, R. Krücken, T.L. Bleis, M. Winkel, European Physical Journal A 49 (2013).
- [25] M. Winkel, Implementierung und Erprobung einer digitalen Pulsformanalyse zur Auslese von Kalorimetern (Diploma thesis), Technische Universität München, 2011.
- [26] H.G. Essel, N. Kurz, IEEE Transactions on Nuclear Science NS-47 (2000) 337.
- [27] P. Rimmels, Development and integration of a freely programmable pulse-generator for the CALIFA calorimeter (Diploma thesis), Technische Universität München, 2015.
- [28] Bronowice Cyclotron Centre, IFJPAN, Krakow, Poland, (www.ifj.edu.pl/ccb).
- [29] GSI, ATIMA, (<https://web-docs.gsi.de/~weick/atima>).
- [30] G. Knoll, Radiation Detection and Measurement, Wiley, Bognor Regis, 2000.
- [31] Y. Koba, H. Iwamoto, K. Kiyohara, T. Nagasaki, G. Wakabayashi, Y. Uozumi, N. Matsufuji, Progress in Nuclear Science and Technology 1 (2011) 218.
- [32] W.M. Yao, et al., Journal of Physics G: Nuclear and Particle Physics 33 (2006) 1.
- [33] J.B. Birks, Proceedings of the Physical Society: Section A 64 (1951) 874.
- [34] The National Institute of Standards and Technology (NIST), PSTAR program, (<http://physics.nist.gov/PhysRefData/Star/Text/PSTAR.html>).
- [35] R.B. Murray, A. Meyer, Physical Review 122 (1961) 815.
- [36] R. Gwin, R. Murray, Studies of the Scintillation Process in CsI(Tl), 1962.
- [37] R. Gwin, R.B. Murray, Physical Review 131 (1963) 501.
- [38] S. Kubota, F. Shiraishi, Y. Takami, Journal of the Physical Society of Japan 69 (2000) 3435.
- [39] M. Pärlog, B. Borderie, M. Rivet, G. Tăbăcaru, A. Chbihi, M. Elouardi, N. L. Neindre, O. Lopez, E. Plagnol, L. Tassan-Got, G. Auger, C. Bacri, N. Bellaïze, F. Bocage, R. Bougault, B. Bouriquet, R. Brou, P. Buchet, J. Charvet, J. Colin, D. Cussol, R. Dayras, A. Demeyer, D. Doré, D. Durand, J. Frankland, E. Galichet, E. Genouin-Duhamel, E. Gerlic, S. Hudan, D. Guinet, P. Lattes, F. Lavaud, J. Lavoie, J. Lecolley, C. Leduc, R. Legrain, M. Louvel, A. Maskay, L. Nalpas, J. Normand, J. Péter, E. Rosato, F. Saint-Laurent, J. Steckmeyer, B. Tamain, O. Tittel, E. Vient, C. Volant, J. Wieleczko, Nuclear Instruments and Methods in Physics Research Section A: Accelerators, Spectrometers, Detectors and Associated Equipment 482 (2002) 674.
- [40] L. Swiderski, M. Szawlowski, M. Mozyński, A. Para, W. Czarnacki, M. Grodzicka, J. Iwanowska-Hanke, M. Kisieliński, J. Wojtkowska, Common Approach to Study Scintillators Response to Gamma-rays and Protons, In: IEEE NSS-MIC, Conference, 2014.
- [41] NIST, Physical Reference Data, X-ray Mass Coefficients, (<http://physics.nist.gov/PhysRefData/XrayMassCoef/ComTab/cesium.html>).